

Spin dynamics in $\text{IrSr}_2\text{Sm}_{1.15}\text{Ce}_{0.85}\text{Cu}_2\text{O}_{10}$: Complex magnetic behavior in a layered iridocuprate

R. H. Colman,¹ P. Manuel,² D. D. Khalyavin,² A. D. Hillier,² and A. C. Mclaughlin^{1,*}

¹*Department of Chemistry, University of Aberdeen, Meston Walk, Aberdeen AB24 3UE, United Kingdom*

²*ISIS Facility, STFC Rutherford Appleton Laboratory, Chilton, Didcot, Oxfordshire OX11 0QA, United Kingdom*

(Received 11 July 2012; revised manuscript received 6 August 2013; published 12 November 2013)

A muon spin rotation (μSR), neutron, and synchrotron diffraction study of the reentrant spin-glass material $\text{IrSr}_2\text{Sm}_{1.15}\text{Ce}_{0.85}\text{Cu}_2\text{O}_{10}$ is presented. The synthesis has been optimized, and Rietveld refinement of the diffraction patterns shows no sign of the previously reported Ir/Cu cation exchange but confirms the structure along with the disordered tilts and rotations of IrO_6 octahedra. The zero-field- μSR response indicates a complex temperature dependence to the magnetism with multiple transitions that are confirmed to be bulk phenomena. Consecutive transitions are reported at $t_1 = 140$, $t_2 = 20$, and $t_3 = 6$ K. The broad transition at 140 K is assigned to antiferromagnetic ordering of Ir^{4+} spins with a stripe spin structure. The low-temperature transitions are a result of antiferromagnetic ordering of Cu^{2+} spins followed by the freezing of a disordered Ir spin component, further evidenced by a strong damping of the oscillation amplitude below 6 K. These observations confirm the bulk nature of the previously reported reentrant spin-glass behavior of this complex magnetic system.

DOI: [10.1103/PhysRevB.88.184408](https://doi.org/10.1103/PhysRevB.88.184408)

PACS number(s): 75.50.Lk, 75.10.Nr, 76.75.+i, 75.47.Lx

I. INTRODUCTION

Cuprate materials have been intensively studied over the past two decades due to the observation of high-temperature superconductivity.¹ More recently, other unexpected physical phenomena, such as low-temperature magnetoresistance have been reported.² The 1212- and 1222-layered cuprate families are ideal structural motifs to search for new phenomena caused by strong spin-charge coupling due to both the flexibility towards cationic substitution and the proximity of the substituted cations to the CuO_2 planes. The 1212- and 1222-layered cuprates have the general formulas $MA_2RCu_2O_{8-\delta}$ and $MA_2R_2Cu_2O_{10-\delta}$ respectively, where M commonly is a transition or p -block metal, A is an alkaline-earth ion, and R is a rare-earth or mixture of rare-earth ions. The broad range of M cations acceptable for substitution into the 1212 and 1222 structures has led to the observation of a variety of magnetic ground-state properties. It is the interaction between these magnetically active ions and the finely balanced electronics of the CuO_2 plane that drives unexpected phenomena in this class of materials.

The underdoped 1222 ruthenocuprates $\text{RuSr}_2\text{R}_{2-x}\text{Ce}_x\text{Cu}_2\text{O}_{10-\delta}$ ($R = \text{Nd, Sm, Eu, and Gd}$) exhibit coexisting superconductivity, weak ferromagnetic order,³ and a sizable magnetoresistance⁴⁻⁷ (MR) at low temperatures. The variation in negative MR with temperature and field are characteristic of charge transport by magnetopolarons—small ferromagnetic regions surrounding each Cu hole within a matrix of antiferromagnetically ordered Cu^{2+} spins.⁸ An applied magnetic field cants the Ru spins into a ferromagnetic arrangement, which induces partial ferromagnetism in the CuO_2 planes, thereby increasing the mobility of the magnetopolarons, giving the observed negative MRs. Surprisingly, this magnetoresistance is found to be tunable from negative to positive values as $\langle r_A \rangle$, the mean- A site ($R_{1.1}\text{Ce}_{0.9}$) cation radius, decreases in a series of $\text{RuSr}_2\text{R}_{0.9}\text{Ce}_{0.9}\text{Y}_{0.2}\text{Cu}_2\text{O}_{10-\delta}$ ($R = \text{Nd, Sm, Eu, and Gd}$) samples.⁹ This lattice effect is further evidenced from studies of $\text{Ru}_{1-x}\text{Ta}_x\text{Sr}_2\text{Nd}_{0.95}\text{Y}_{0.15}\text{Ce}_{0.9}\text{Cu}_2\text{O}_{10}$ materials; $\text{MR}_{9\text{T}}$ (4 K) increases from -28% to -49% as x increases from

0 to 0.2, which further expands the unit cell. The ruthenium order has also been seen to induce an unconventional ordering of Cu moments within the pseudogap region of the hole-doped cuprate phase diagram.^{4,5}

The 1222-series $\text{CoSr}_2\text{Y}_{2-x}\text{Ce}_x\text{Cu}_2\text{O}_{9\pm\delta}$ ($x = 0.5-0.8$) has also been reported; there is no evidence for superconductivity, but antiferromagnetic order of the Co^{3+} spins is observed.¹⁰ Similar magnetic properties are reported for the 1212 analog, and results show that, with increased Ca doping in $\text{CoSr}_2\text{Y}_{1-x}\text{Ca}_x\text{Cu}_2\text{O}_7$ ($x = 0-0.4$),¹¹ negative MR is observed for $\text{CoSr}_2\text{Y}_{0.6}\text{Ca}_{0.4}\text{Cu}_2\text{O}_7$ [$\text{MR}_{14\text{T}}$ (35 K) = -14%]. The Cr analog has thus far been synthesized in the 1212-structure $\text{CrSr}_2\text{RCu}_2\text{O}_8$ ($R = \text{La, Pr, Nd, Eu, Gd, Tb, Dy, Y, Ho, Er, and Lu}$) (Ref. 12) where antiferromagnetic order of the Cr^{4+} spins is reported at ~ 130 and 150 K for $R = \text{Y}$ and La , respectively. Magnetotransport properties are yet to be reported for these materials. The 1222-iridocuprate $\text{Ir}_{0.85}\text{Sr}_2\text{Sm}_{1.15}\text{Ce}_{0.85}\text{Cu}_{2.15}\text{O}_{10}$ has recently been synthesized and is reported to show both low-temperature negative magnetoresistance, reminiscent of the ruthenocuprates, and a complex set of magnetic ordering transitions assigned to reentrant spin-glass behavior (RSG).^{13,14} Magnetic spin-glass-like behaviors have also been seen in susceptibility measurements of the 1212-iridocuprates $\text{IrSr}_2\text{SmCu}_2\text{O}_8$ and $\text{IrSr}_2\text{EuCu}_2\text{O}_8$ (Refs. 15 and 16), but the 1212 iridocuprates are only found to be synthesizable under elevated pressure, reducing available sample quantity and purity.¹⁷

In this paper, we report an optimized synthesis protocol, high quality synchrotron x-ray and neutron-diffraction refinements, muon spin relaxation spectroscopy (μSR) analysis, and dc-susceptibility measurements for the 1222-iridocuprate $\text{IrSr}_2\text{Sm}_{1.15}\text{Ce}_{0.85}\text{Cu}_2\text{O}_{10}$. The μSR analysis confirms the bulk nature of multiple magnetic transitions in this complex material so that magnetic ordering of the Ir^{4+} ions is evidenced at 140 K, followed by freezing-in of a disordered component to the Ir magnetic order at low temperature. This disordered component is a result of the magnetic exchange frustration presently brought about by the disordered occupation of mixed $\text{Ir}^{4+}/\text{Ir}^{5+}$ in this material. The Cu spins are shown to order antiferromagnetically at 20 K.

II. EXPERIMENT

$\text{IrSr}_2\text{Sm}_{1.15}\text{Ce}_{0.85}\text{Cu}_2\text{O}_{10}$ was prepared by solid-state reaction of stoichiometric powders IrO_2 , SrCO_3 , Sm_2O_3 , CeO_2 , and CuO . After combination by thorough grinding, the mixture was pressed into a 10-mm pellet and was prereacted in air at 800°C for 10 h. The pellet then was reground and was repressed into a pellet before being heated to 1042°C in a slow-flowing oxygen atmosphere for ~ 1200 h with multiple regrinds. A $5^\circ\text{C}/\text{min}$ heating and cooling rate was used in all steps. This increased reaction time and slightly elevated temperature was found to produce samples with much lower impurity fractions than the reaction protocol previously reported.¹³

Magnetic susceptibility measurements were performed on a Quantum Design magnetic property measurements system (MPMS) with the vibrating sample magnetometer mode in a 100-Oe field upon zero-field cooling (ZFC) and field cooling (FC). The electronic transport properties of a sintered ceramic bar of $\text{IrSr}_2\text{Sm}_{1.15}\text{Ce}_{0.85}\text{Cu}_2\text{O}_{10}$ were investigated using a Quantum Design physical property measurement system. The resistivity of the bar was measured using the four-point probe technique as a function of temperature in the range of $4 < T < 350$ K in both a zero applied field and a 7-T applied field.

Synchrotron x-ray-diffraction patterns were collected using beamline I11 at the Diamond Light Source, United Kingdom. The sample was mounted on the surface of a 0.2-mm borosilicate capillary tube. Collections were performed at room temperature in the angular range of $0.5^\circ < 2\theta < 150^\circ$ with a step size of $0.001^\circ 2\theta$ and $\lambda = 0.827124 \text{ \AA}$.

Variable-temperature neutron-diffraction patterns were recorded on the WISH diffractometer on the second target station (TS-2) at the ISIS pulsed neutron and muon source, United Kingdom. A 1-g sample of isotopically enriched $\text{Ir}_{0.85}\text{Sr}_2^{154}\text{Sm}_{1.15}\text{Ce}_{0.85}\text{Cu}_{2.15}\text{O}_{10}$ was loaded into a vanadium can, and data were recorded at 2, 20, 30, 60, 80, 120, 140, 200, and 290 K for 2 h at each temperature. The magnetic form-factor parameters for Ir ions used in the refinement were taken from recent pseudorelativistic Hartree-Fock calculations.¹⁸

The μSR measurements were performed using the EMU spectrometer at the ISIS pulsed neutron and muon source, United Kingdom. A 3.5-g sample of $\text{IrSr}_2\text{Sm}_{1.15}\text{Ce}_{0.85}\text{Cu}_2\text{O}_{10}$ was loaded onto a silver plate and was mounted in an Oxford Instruments Variox cryostat for cooling. In a μSR experiment, spin-polarized positive muons μ^+ are implanted into the sample and come to rest at sites of electrostatic minimum, commonly near the oxygen position in oxides. The muon spins begin to precess about the magnetic field experienced at the stopping site and, after an average lifetime of $2.2\text{-}\mu\text{s}$ decay, emit a positron preferentially along the spin direction of the muon at the time of decay. Emitted positrons are detected in either forwards or backwards detectors with respect to the initial muon polarization direction, and the asymmetry is defined by the equation,

$$G_Z(t) = (N_F - \alpha N_B)/(N_F + \alpha N_B), \quad (1)$$

where N_F and N_B are the total counts in forwards and backwards detectors, respectively, and α is a calibration constant correcting for detector efficiencies and sample environment. Additional to the signal from the sample, muons implanted into

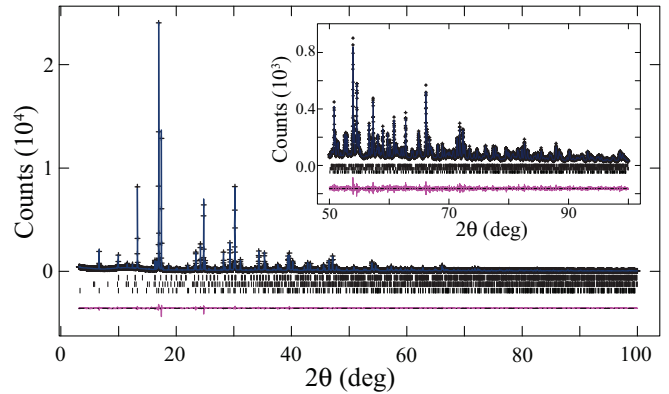


FIG. 1. (Color online) Rietveld refinement of synchrotron x-ray data collected on $\text{IrSr}_2\text{Sm}_{1.15}\text{Ce}_{0.85}\text{Cu}_2\text{O}_{10}$ using beamline I11 at the Diamond Light Source, United Kingdom. Crosses represent the data, the line is the fit, and the lower line is the difference curve. Tick marks represent reflection positions for $\text{IrSr}_2\text{Sm}_{1.15}\text{Ce}_{0.85}\text{Cu}_2\text{O}_{10}$ and $\text{Sr}_4\text{CuIr}_2\text{O}_9$ (1.4 wt %) and $\text{Sr}_2(\text{Sm,Ce})\text{IrO}_6$ (4.5 wt %) minor impurity phases from top to bottom, respectively. The inset is a zoom of the high angle data and the final goodness of fit $\chi^2 = 2.257$.

the silver sample holder give rise to a time- and temperature-independent background asymmetry, which was fitted at low temperatures to give a value of $A_{\text{background}} = 2.06\%$. All muon spectral fits were performed using the WIMDA analysis suite.¹⁹

III. RESULTS AND DISCUSSION

A. Synchrotron x-ray diffraction

To confirm the crystal structure and phase purity, a Rietveld refinement of the x-ray diffraction data collected on I11 was performed using the GSAS software package.²⁰ As with other 1222-layered cuprates, the diffraction pattern is best indexed by the tetragonal $I4/mmm$ space group with lattice parameters of $a = 3.855885(6)$ and $b = 28.55983(6) \text{ \AA}$. The data and resulting fit can be seen in Fig. 1, and the fitted parameters are summarized in Table I. In addition to the intended $\text{IrSr}_2\text{Sm}_{1.15}\text{Ce}_{0.85}\text{Cu}_2\text{O}_{10}$ phase, unindexed reflections were noted that could be assigned to the minor impurity phases $\text{Sr}_2(\text{Ce,Sm})\text{IrO}_6$ and $\text{Sr}_4\text{CuIr}_2\text{O}_9$. Upon inclusion in the refinement, the phase weight fractions of these impurities refine to 4.6(1)% and 1.5(1)%, respectively, such levels of impurities are commonly reported for 1222 materials.³⁻⁹ These minor impurity phases do not exhibit magnetic transitions coincident with those reported below.

This 1222-iridocuprate structure can be described as alternating layers of IrO_2 , SrO , CuO_2 , Sm/Ce , O_2 , Sm/Ce , CuO_2 , SrO , and IrO_2 , respectively. As with all 1222 materials, the Sm^{3+} and Ce^{4+} ions are distributed at random over the cation sites within the fluorite, $(\text{Sm,Ce})_2\text{O}_2$ block. A bond-length mismatch between the CuO_2 and IrO_2 planes [$r_{\text{CuO}(2)} = 1.9298(1)$ and $r_{\text{IrO}(3)} = 2.0003(10) \text{ \AA}$, respectively] is accommodated in these materials through a disordered tilting and rotation of the IrO_6 octahedra. If these tilts and rotations were ordered, superstructure reflections would become apparent due to the symmetry breaking of the parent $I4/mmm$ space group. No superstructure peaks are seen, and the data can be well modeled by allowing both O(1) and O(3)

TABLE I. Refined structural parameters for IrSr₂Sm_{1.15}Ce_{0.85}Cu₂O₁₀ in the space-group *I4/mmm* from Rietveld refinement of synchrotron x-ray diffraction data using beamline I11 of the Diamond Light Source, United Kingdom.

<i>a</i> (Å)	<i>c</i> (Å)	Volume (Å ³)	<i>R</i> _{wp}	<i>R</i> _p	χ ²	<i>U</i> _{iso} (Å ²)	<i>U</i> ₁₁ (Å ²) ^a	<i>U</i> ₃₃ (Å ²) ^a
atom(s)	Wyckoff site	<i>x</i>	<i>y</i>	<i>z</i>	occupancy			
Ir	2 <i>a</i>	0	0	0	1		0.0084(1)	0.0053(2)
Sr	4 <i>e</i>	0.5	0.5	0.07851(2)	1		0.0129(2)	0.0127(2)
Sm,Ce	4 <i>e</i>	0.5	0.5	0.20487(1)	0.575,0.425		0.0033(1)	0.0039(1)
Cu	4 <i>e</i>	0	0	0.14394(2)	1		0.0024(1)	0.0024(3)
O(1)	16 <i>m</i>	0.963(2)	0.963(2)	0.0698(1)	0.25	0.016(2)		
O(2)	8 <i>g</i>	0	0.5	0.1469(1)	1	0.0096(4)		
O(3)	8 <i>j</i>	0.8618(10)	0.5	0	0.5	0.0135(12)		
O(4)	4 <i>d</i>	0	0.5	0.25	1	0.001(5)		

^aAll of the anisotropically refined sites have $U_{11} = U_{22} \neq U_{33}$ and $U_{12} = U_{13} = U_{23} = 0$.

to reside at positions of lower symmetry, adjusting the site fractions accordingly. The resulting fitted oxygen positions give rise to a disordered 15.5(1)° rotation and 5.7(4)° tilting of the octahedra, in agreement with that previously reported.¹³

In contrast to work previously published, no evidence was found for the incorporation of Cu onto the nominal Ir position (2*a* Wyckoff site). The revised synthetic protocol described in this paper repeatedly gives rise to samples of lower impurity phase content to that previously described. As a result, the stoichiometric balance of reactant materials is more rigorously maintained throughout the reaction, reducing the drive for substitution between electrostatically unfavorable sites, such as the Cu^{2+,3+} ↔ Ir^{5+,4+} exchange.

B. Muon spin relaxation spectroscopy

The zero-field muon response is seen to develop several distinct features upon cooling from 300 K to the base temperature of the cryostat 1.5 K (Fig. 2). In order to capture the complexity of this response, the following function [Eq. (2)] was used to fit the data,

$$G_z(t) = A_1 e^{-\lambda_1 t} + A_2 e^{-\lambda_2 t} + A_3 e^{[-(\sigma^2 t^2)/2]} \cos(\gamma_u B_u + \Phi). \quad (2)$$

This function can be considered a combination of three separate contributions to the spectra, each arising from distinct electronic origins, and so, each can be considered independently. The temperature regions where each contribution is significant, the physical implications, and the fitted parameters will be discussed in the following sections.

In the high-temperature regime (300 K > *T* > 140 K), the spectra can be well fitted by a single exponential relaxation function,

$$G_z(t) = A_1 e^{-\lambda_1 t}, \quad (3)$$

where *A*₁ represents the initial asymmetry of the function and λ₁ is the muon depolarization rate. This relaxation behavior commonly arises due to the interaction between the muon spins and a dynamic electronic response, partially depolarizing the muons. The depolarization rate of the muons λ₁ is low, showing that the spin dynamics are comparatively fast and interacting weakly with the muons. Only a slight increase in depolarization and, therefore, slowing of the spin dynamics is

seen while cooling through this temperature region (Fig. 3). No significant loss of initial asymmetry *A*₁ (Fig. 4) is seen, suggesting that all of the muons are being observed and no transition to an ordered or frozen state has occurred.

Upon cooling through the region of 140 K > *T* > 60 K, the spectra can no longer be well modeled using a single relaxation function due to the observance of a fast relaxing component at short times in addition to the slower relaxing component already observed. Attempts to model this with a single stretched-exponential function did not fully capture the spectral shape. The additional component, however, can be well modeled by adding a second relaxing term in the fitting function,

$$G_z(t) = A_1 e^{-\lambda_1 t} + A_2 e^{-\lambda_2 t}. \quad (4)$$

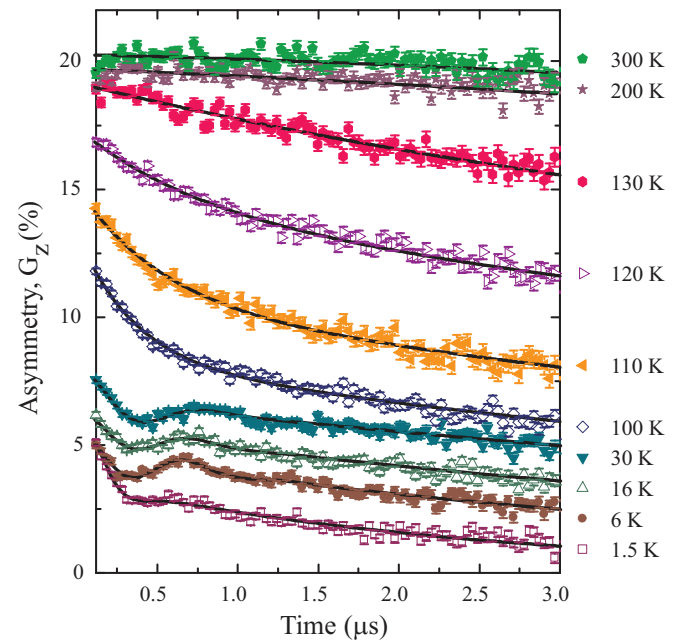


FIG. 2. (Color online) Temperature-dependent muon spin relaxation spectra showing a reduction in initial asymmetry upon cooling as well as a complex temperature dependence for the line shape. Solid lines show fits to the data.

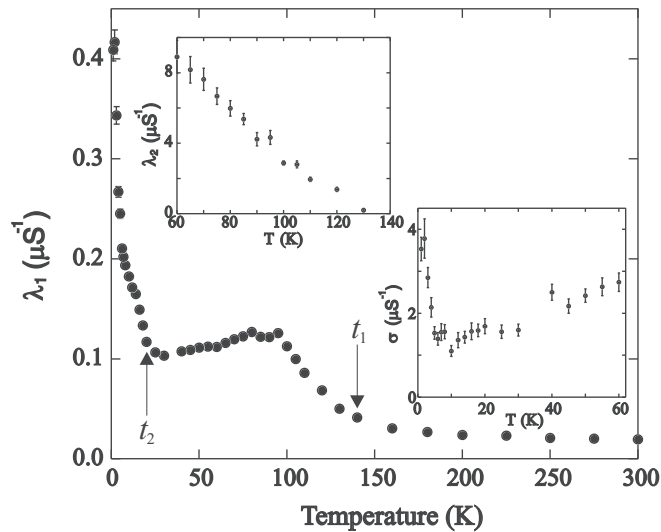


FIG. 3. Temperature dependence of the fitted muon depolarization rates λ_1 , λ_2 (inset), and σ (inset). A steep increase in depolarization is observed in λ_1 upon cooling below 140 K, indicating an initial magnetic transition t_1 . At lower temperatures, two further changes in slope at 20 K (t_2) and 6 K (t_3) indicate consecutive changes in the bulk magnetic state.

The observation of two distinct relaxation behaviors in Eq. (4) indicates the presence of two muon stopping sites within the structure, experiencing different internal field strengths. At high temperatures, the relaxation behavior of the two sites is too similar to deconvolute their individual

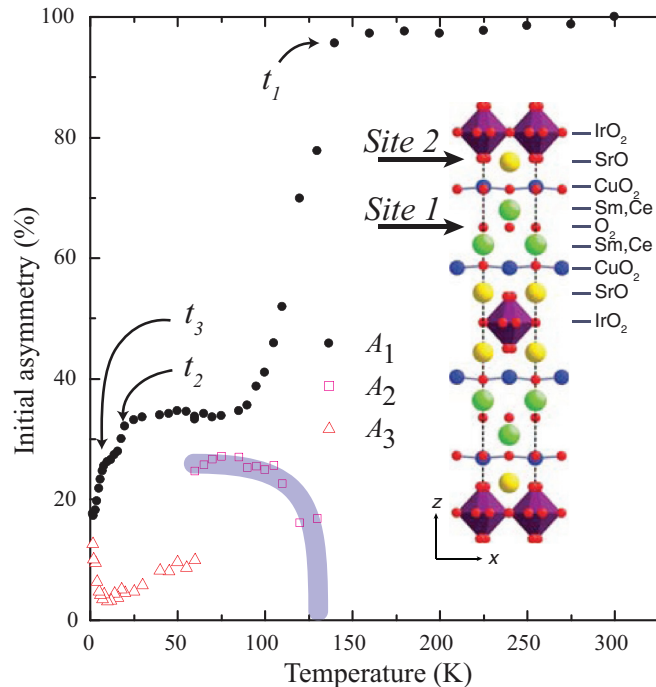


FIG. 4. (Color online) Temperature dependence of the fitted initial asymmetry of each component A_1 , A_2 , and A_3 normalized to the 300-K asymmetry. The initial drop in cooling below 140 K confirms the bulk nature of the transition. The inset is the crystal structure, showing the layered nature, and arrows indicate the likely oxygen planes containing the two muon stopping sites.

contributions, but upon cooling, the depolarization of muons at the second site λ_2 (inset Fig. 3) increases significantly more quickly. The initial asymmetry associated with muons at this site is seen to initially increase as the two sites become more easily distinguished, followed by a plateau once the two sites are fitted successfully as distinct contributions to the spectra (Fig. 4). The large depolarization rate and loss of asymmetry associated with muons at this stopping site (λ_2, A_2) suggest that they are more intimately coupled to the electronic behavior of the magnetically active ions than the stopping site associated with λ_1 and A_1 . Comparisons with a previous μ SR study of the 1222-ruthenocuprate $\text{RuSr}_2\text{Eu}_{1.4}\text{Ce}_{0.6}\text{Cu}_2\text{O}_{10}$ suggest that the most likely stopping sites are as follows: sandwiched between the rare-earth ion layers in the fluorite block, labeled as *site 1* in Fig. 4 (λ_1, A_1), and close to the oxygen bridging the magnetically active Ir and Cu ions, labeled as *site 2* (λ_2, A_2).²¹ The difference in experienced fields expected for muons at these two sites, due to the proximities to magnetically active ions, fits well with the large observed differences in muon relaxation rates for these two distinct sites in $\text{IrSr}_2\text{Sm}_{1.15}\text{Ce}_{0.85}\text{Cu}_2\text{O}_{10}$. Below 60 K, the relaxation at *site 2* is no longer observable within the time window of the pulsed-source spectrometer, i.e., the depolarization of the muons occurs in a time scale of less than 0.12 μs .

Figures 2 and 4 show that accompanying the change in λ_1 and λ_2 is a significant loss of initial asymmetry A_1 , indicative of muons experiencing either a disordered frozen magnetic state or a magnetically ordered state with a frequency of precession outside the spectrometer time window and, hence, no observation of an oscillating component. This transition is evident in the magnetic susceptibility data where a weak broad anomaly is observed below 140 K with splitting of the ZFC and FC data. Upon cooling to 60 K, an oscillation is clearly observed (Fig. 5), which is indicative of a coherent ordered magnetic component. This suggests that the 140-K transition is due to a magnetically ordered state rather than a disordered

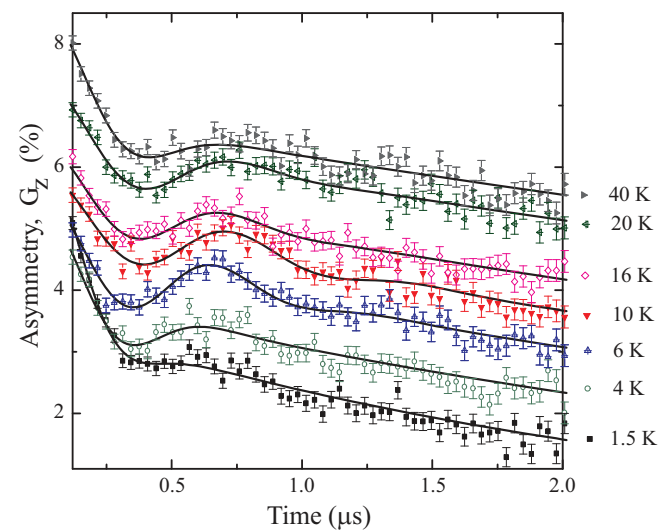


FIG. 5. (Color online) Low-temperature muon relaxation spectra showing the development of an oscillating component below 60 K. Solid lines show fits to the data. A decrease in oscillation amplitude upon cooling below 6 K suggests the onset of a disordered frozen component in the magnetic ground state.

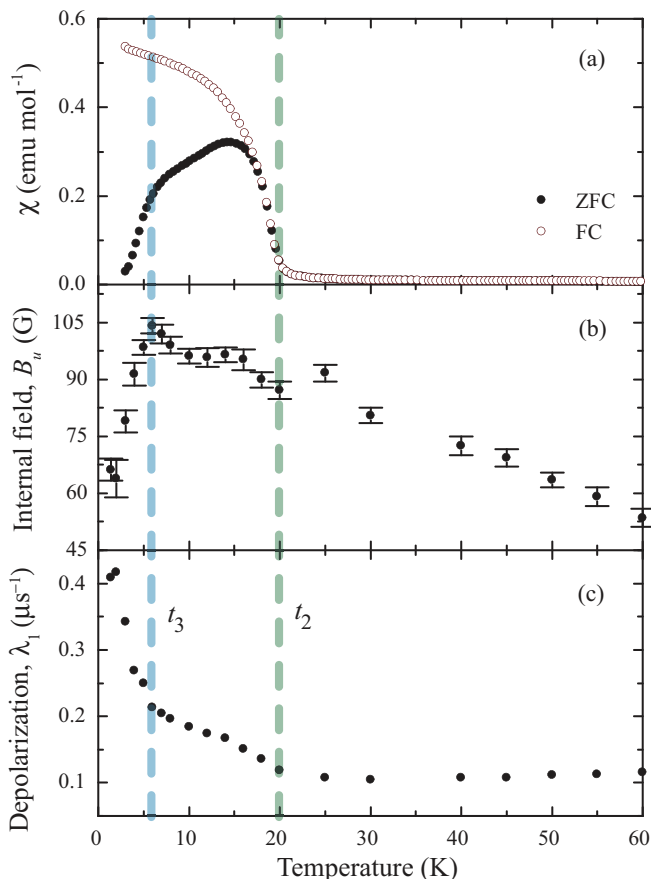


FIG. 6. (Color online) (a) Magnetic susceptibility of IrSr₂Sm_{1.15}Ce_{0.85}Cu₂O₁₀ measured in a 100-Oe field after both ZFC and FC, (b) the fitted internal field at the muon stopping site B_u , and (c) low-temperature fitted depolarization rate λ_1 . The temperature dependence of these three distinct plots show concomitant features that confirm the bulk nature of two distinct low-temperature transitions t_2 and t_3 at 20 and 6 K, respectively.

frozen magnetic transition. To successfully fit this oscillation, the following function was adopted for the temperature range of 60 K $>$ $T >$ 1.5 K:

$$G_z(t) = A_1 e^{-\lambda_1 t} + A_3 e^{[-(\sigma^2 t^2)/2]} \cos(\gamma_u B_u + \Phi), \quad (5)$$

where σ is the muon depolarization rate, the frequency of the oscillation is defined by the gyromagnetic ratio of the muon $\gamma_u/2\pi = 135.538 \text{ MHz s}^{-1} \text{ T}^{-1}$, and the experienced internal field at the muon site B_u plus an arbitrary phase shift Φ . The amplitude of the observed oscillation is quickly damped, indicating a distribution of fields at the muon site.

Figure 6(b) shows that the internal field B_u increases upon cooling below 60 K to a broad plateau at 20 K (t_2). At this transition, a rise in λ_1 and a reduction in A_1 is also evidenced (Figs. 3, 4, and 6). Upon cooling further, the internal field (B_u), corresponding to the frequency of the oscillation, is seen to peak at 6 K with a sharp drop upon further cooling and a concomitant change in σ [Fig. 3 (inset)] and λ_1 [Figs. 6(b) and 6(c)]. A further drop in the initial asymmetry A_1 and rise in A_3 are also evidenced (Fig. 4). The existence of the two low-temperature transitions t_2 and t_3 at 20 and 6 K is confirmed by

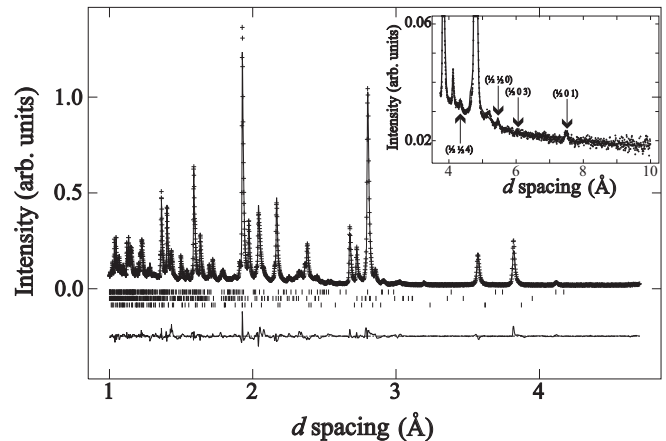


FIG. 7. Rietveld refinement of the neutron-powder-diffraction data collected at 2 K. The cross symbols and the solid line represent the experimental and calculated intensities, respectively, and the line below is the difference between them. The inset shows the positions of magnetic Bragg peaks at 2 K. A small unknown impurity peak is observed at 5.2.

susceptibility measurements where clear divergence between the ZFC and the FC susceptibilities is observed below 20 K followed by a sharp drop in the ZFC susceptibility below 6 K [Fig. 6(a)].

Variable-temperature neutron-diffraction data show that, upon cooling to 2 K, there is no change in crystal symmetry as an excellent fit to the $I4/mmm$ space group is obtained [Fig. 7; $a = 3.8497(1)$; $c = 28.5244(11)$; $R_{wp} = 7.69\%$; $R_p = 7.42\%$]. Upon cooling to 140 K, two very weak magnetic peaks are observed which can be indexed as $(\frac{1}{2} 0 1)$ and $(\frac{1}{2} 0 3)$ so that the propagation vector $k = (\frac{1}{2}, 0, 0)$. The neutron-diffraction data confirm that the $t_1 = 140$ -K transition observed in the μ SR data (Figs. 2–6) arises due to a coherent ordered magnetic component. The magnetic peaks can be modeled by antiferromagnetic order of the Ir⁴⁺ spins in a stripe structure where spins align antiferromagnetically along a and ferromagnetically along b and c . The moment aligns parallel to c and refines to $0.50(5)\mu_B$ at 2 K. The ordering of Ir spins into antiferromagnetic stripes does not break the tetragonal symmetry. The observation of a striped magnetic spin structure in the ab plane, rather than a checkerboard spin structure, suggests that there are strong next-nearest-neighbor (NNN) interactions between Ir spins. The observed magnetic structure is, therefore, most likely a consequence of the presence of both Ir⁴⁺ $J = 1/2$ and diamagnetic Ir⁵⁺ within the crystal lattice, leading to mixed exchange interactions so that the NNN interactions dominate and the magnetic stripe spin structure is stabilized. Upon cooling to 20 K, further magnetic peaks are observed which can be indexed with a $(\frac{1}{2} \frac{1}{2} 0)$ propagation vector. This is suggestive of antiferromagnetic order of the Cu spins in the ab plane with a $(\frac{1}{2} \frac{1}{2} 0)$ superstructure as reported for underdoped ruthenocuprates.^{4,5} An excellent fit to the Cu magnetic superstructure intensities is obtained with a model containing Cu spins aligned antiferromagnetically in the ab plane but ferromagnetically along c . The moment aligns in the basal plane and refines to $0.32(4)$ at 2 K. The Rietveld fit to the magnetic structure of ordered Ir and Cu spins at 2 K is shown in

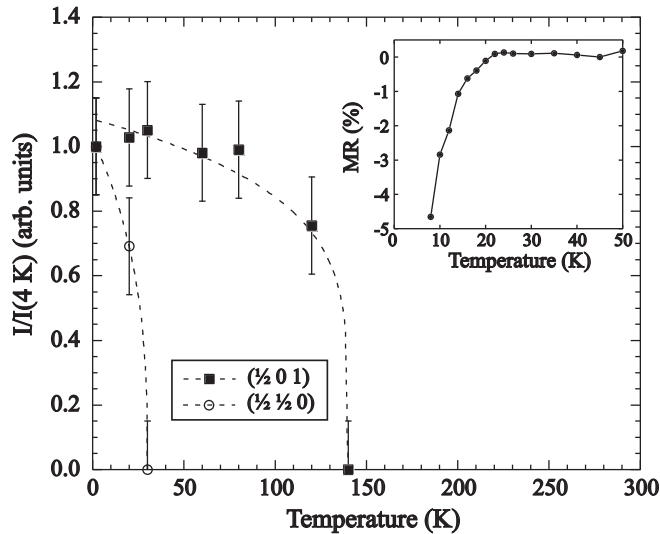


FIG. 8. Integrated intensity of the $(\frac{1}{2} 0 1)$ and $(\frac{1}{2} \frac{1}{2} 0)$ magnetic reflections. Dotted lines are a guide to the eye. The inset shows the variation in negative MR with the temperature for $\text{IrSr}_2\text{Sm}_{1.15}\text{Ce}_{0.85}\text{Cu}_2\text{O}_{10}$ recorded in a 7-T magnetic field.

the inset to Fig. 7. There is no evidence of a third transition in the neutron data upon cooling from 20 to 2 K. The temperature variation in the integrated intensities of the $(\frac{1}{2} 0 1)$ and $(\frac{1}{2} \frac{1}{2} 0)$ magnetic superstructure peaks are displayed in Fig. 8, which shows that $T_N(\text{Ir}) = 140$ K and $T_N(\text{Cu}) < 30$ K so that the second magnetic transition observed in μSR and magnetic susceptibility data (Figs. 3, 4, and 6) is a result of Cu antiferromagnetic order.

RSG behavior commonly is observed in alloys, such as AuFe .²² According to Gabay and Toulouse,²³ in a RSG material, the RSG transition occurs below T_c or T_N where T_N or T_c are the Néel or Curie temperatures, respectively. The RSG transition is a result of a mixed state in which long-range magnetic order in the z direction coexists with frozen-in transverse spin components. In such a RSG system, magnetic Bragg diffraction is still observed.²³ Three transitions are clearly evidenced in the μSR data, and the neutron-diffraction data demonstrate that $t_1 = T_N(\text{Ir}) = 140$ K and $t_2 = T_N(\text{Cu}) \sim 20$ K. The third transition t_3 at 6 K (observable in the magnetic susceptibility and μSR data) is not evidenced in the neutron data so that there is no change in the magnetic structure between 20 and 2 K. This third transition is attributed to a reentrant spin-glass transition so that $T_{\text{RSG}} = 6$ K. The reduction in the internal field at the muon site below 6 K is, therefore, due to the freezing of a disordered component within the existing magnetic structure, lowering the mean-internal field of the site and strongly damping the oscillation. The glassy character of the low-temperature transition has been previously confirmed by ac-susceptibility measurements, showing a characteristic frequency dependence that can be well fitted by the Vogel-Fulcher law.¹³ The observation of reentrant spin-glass behavior in $\text{IrSr}_2\text{Sm}_{1.15}\text{Ce}_{0.85}\text{Cu}_2\text{O}_{10}$ can be well explained by the mixed $\text{Ir}^{4+}/\text{Ir}^{5+}$ valency. Partial Ir^{4+} $J = 1/2$ occupation of an otherwise diamagnetic Ir^{5+} lattice will lead to mixed exchange interactions and, as such,

magnetic frustration. At high temperatures, the dominant exchange terms lead to an initial ordering transition at 140 K, but with further cooling, the weaker competing exchange interactions become large enough to induce a disordered component below 6 K. The combined μSR and susceptibility results reported here confirm the previous assignment of this 1222 iridocuprate as a reentrant spin-glass material where magnetic ordering is clearly observed at 140 K, followed by spin-glass transitions upon cooling. In a reentrant spin glass, the long-range longitudinal order should coexist with the frozen transverse spin components at the lowest temperatures. This is clearly evidenced for $\text{IrSr}_2\text{Sm}_{1.15}\text{Ce}_{0.85}\text{Cu}_2\text{O}_{10}$ where an oscillation is observed in the μSR data and magnetic Bragg peaks are evidenced in the neutron-diffraction data down to 1.5 K.

The variation in MR with temperature for $\text{IrSr}_2\text{Sm}_{1.15}\text{Ce}_{0.85}\text{Cu}_2\text{O}_{10}$ is displayed in the inset to Fig. 8. A small negative magnetoresistance is observed below 22 K as previously reported. Hence the negative MR is only observed below $T_N(\text{Cu})$ so that these results demonstrate that the observed MR is a result of a change in conductivity in the CuO_2 plane upon application of a magnetic field. The charge transport is dominated by magnetopolarons¹⁷—small ferromagnetic regions surrounding each Cu hole within a matrix of antiferromagnetically ordered Cu^{2+} spins.⁸ An applied magnetic field induces partial ferromagnetism in the CuO_2 planes thereby increasing the mobility of the magnetopolarons, giving the observed negative MRs. Magnetopolaron hopping is a thermally activated process, leading to a characteristic exponential rise in negative MR below the Cu spin transition T_{Cu} .

IV. CONCLUSIONS

To summarize, we report a different procedure for the synthesis of $\text{IrSr}_2\text{Sm}_{1.15}\text{Ce}_{0.85}\text{Cu}_2\text{O}_{10}$. Refinement of synchrotron x-ray diffraction data shows that the *improved synthetic protocol* means that there no longer is Ir/Cu mixing on the nominal Ir site. This has a marked influence on the magnetic properties. Incorporation of 17.5(5)% Cu onto the nominal Ir site results in $T_N \sim 120$ K and $T_{\text{RSG}} = 8$ K. Upon achieving cation order between $\text{Ir}^{4+/5+}$ and Cu^{2+} sites, T_N increases to 140 K, and T_{RSG} decreases to 6 K. Antiferromagnetic order of the Cu^{2+} spins is also observed at ~ 20 K. The magnetic exchange frustration present in this material is due to mixed $\text{Ir}^{4+}/\text{Ir}^{5+}$ occupation of the IrO_2 plane, which is likely to easily be destabilized by incorporation of even slight amounts of Cu^{3+} onto the lattice.

ACKNOWLEDGMENTS

We acknowledge EPSRC for the provision of research Grant No. EP/F035225 and STFC for the provision of beam time at the Diamond Light Source and the ISIS pulsed neutron and muon source. We would also like to thank Professor C. Tang for assistance with the synchrotron x-ray-diffraction experiments and Dr. A. Dobrynin for time on the MPMS.

*a.c.mclaughlin@abdn.ac.uk

- ¹J. G. Bednorz and K. A. Müller, *Z. Phys. B* **64**, 189 (1986).
- ²Y. Ando, A. N. Lavrov, and S. Komiya, *Phys. Rev. Lett.* **90**, 247003 (2003).
- ³A. C. McLaughlin, I. Felner, and V. P. S. Awana, *Phys. Rev. B* **78**, 094501 (2008).
- ⁴A. C. McLaughlin, F. Sher, and J. P. Attfield, *Nature (London)* **436**, 829 (2005); **437**, 1057(E) (2005).
- ⁵A. C. McLaughlin, F. Sher, S. A. J. Kimber, and J. P. Attfield, *Phys. Rev. B* **76**, 094514 (2007).
- ⁶A. C. McLaughlin and J. P. Attfield, *J. Magn. Magn. Mater.* **310**, 1961 (2007).
- ⁷A. C. McLaughlin, L. Begg, A. J. McCue, and J. P. Attfield, *Chem. Commun. (Cambridge)* **22**, 2273 (2007).
- ⁸E. L. Nagaev, *JETP Lett.* **6**, 18 (1967).
- ⁹A. C. McLaughlin, L. Begg, C. Harrow, S. A. J. Kimber, F. Sher, and J. P. Attfield, *J. Am. Chem. Soc.* **128**, 12364 (2006).
- ¹⁰A. C. McLaughlin, D. Morrice, and F. Sher, *J. Solid State Chem.* **178**, 2274 (2005).
- ¹¹X. G. Luo, X. H. Chen, X. Liu, R. T. Wang, Y. M. Xiong, C. H. Wang, G. Y. Wang, and X. G. Qiu, *Phys. Rev. B* **70**, 054520 (2004).
- ¹²R. Ruiz-Bustos, M. H. Aguirre, and M. A. Alario-Franco, *Inorg. Chem.* **44**, 3063 (2005).
- ¹³R. H. Colman and A. C. McLaughlin, *Phys. Rev. B* **85**, 144419 (2012).
- ¹⁴I. Mirebeau, S. Itoh, S. Mitsuda, T. Watanabe, Y. Endoh, M. Hennion, and R. Papoular, *Phys. Rev. B* **41**, 11405 (1990).
- ¹⁵A. J. Dos Santos Garcia, A. M. Arevalo-Lopez, J. Fernandez-Sanjulian, M. A. Alario-Franco, and D. Frost, *High Press. Res.* **30**, 17 (2010).
- ¹⁶A. J. Dos Santos Garcia, M. H. Aguirre, R. Saex Puche, and M. A. Alario-Franco, *J. Solid State Chem.* **179**, 1296 (2006).
- ¹⁷A. J. Dos Santos Garcia, R. Ruiz-Bustos, A. M. Arevalo-Lopez, and M. A. Alario-Franco, *High Press. Res.* **28**, 525 (2008).
- ¹⁸K. Kobayashi, T. Nagao, and M. Ito, *Acta Crystallogr., Sect. A: Cryst. Phys., Diffr., Theor. Gen. Crystallogr.* **67**, 473 (2011).
- ¹⁹F. L. Pratt, *Physica B* **289–290**, 710 (2000).
- ²⁰A. C. Larson and R. B. Von Dreele, Los Alamos National Laboratory Report LAUR No. 86, 2004 (unpublished).
- ²¹A. Shengalaya, R. Khasanov, D. G. Eschenko, I. Felner, U. Asaf, I. M. Savić, H. Keller, and K. A. Müller, *Phys. Rev. B* **69**, 024517 (2004).
- ²²B. H. Verbeek and J. A. Mydosh, *J. Phys. F* **8**, L109 (1978).
- ²³M. Gabay and G. Toulouse, *Phys. Rev. Lett.* **47**, 201 (1981).